

# Capturing reduced-order quantum many-body dynamics out of equilibrium via neural ordinary differential equations

Patrick Egenlauf<sup>1,\*</sup>, Iva Březinová<sup>2</sup>, Sabine Andergassen<sup>3,4</sup>, and Miriam Klopotek<sup>1,5</sup>

<sup>1</sup>Stuttgart Center for Simulation Science, Cluster of Excellence EXC 2075, University of Stuttgart, Universitätsstraße 32, 70569 Stuttgart, Germany

<sup>2</sup>Institute for Theoretical Physics, Vienna University of Technology, Wiedner Hauptstraße 8-10, A-1040 Vienna, Austria

<sup>3</sup>Institute of Information Systems Engineering, Vienna University of Technology, 1040 Vienna, Austria

<sup>4</sup>Institute of Solid State Physics, Vienna University of Technology, 1040 Vienna, Austria

<sup>5</sup>WIN-Kolleg of the Young Academy | Heidelberg Academy of Sciences and Humanities, Karlstraße 4, 69117 Heidelberg, Germany

December 17, 2025

## Abstract

Out-of-equilibrium quantum many-body systems – such as multi-electron atoms and molecules driven by strong laser fields, quenched ultracold gases, and ultrafast-excited solids – exhibit rapid correlation buildup that underlies many emerging phenomena. Exact wave-function methods to describe this scale exponentially with particle number; simpler mean-field approaches neglect essential two-particle correlations. The time-dependent two-particle reduced density matrix (TD2RDM) formalism offers a middle ground by propagating the two-particle density matrix and closing the Bogoliubov–Born–Green–Kirkwood–Yvon (BBGKY) hierarchy with a reconstruction of the three-particle cumulant. But the validity and existence of time-local reconstruction functionals ignoring memory effects remain unclear across different dynamical regimes. We show that a neural ordinary differential equation (ODE) model trained on exact two-particle reduced density matrix (2RDM) data (no dimensionality reduction) can reproduce its full dynamics without any explicit three-particle information – but only in parameter regions where the Pearson correlation between the two- and three-particle cumulants is large. In contrast, in the anti-correlated or uncorrelated regime, the neural ODE fails, indicating that no simple time-local functional of the instantaneous two-particle cumulant can capture the evolution. The magnitude of the time-averaged three-particle-correlation buildup appears to be the primary predictor of success: For a moderate correlation buildup, both neural ODE predictions and existing TD2RDM reconstructions are accurate, whereas stronger values lead to systematic breakdowns. These findings pinpoint the need for memory-dependent kernels in the three-particle cumulant reconstruction for the latter regime. Our results place the neural ODE as a model-agnostic diagnostic tool that maps the regime of applicability of cumulant expansion methods and guides the development of non-local closure schemes. More broadly, the ability to learn high-dimensional reduced-density-matrix dynamics from limited data opens a pathway to fast, data-driven simulation of correlated quantum matter, complementing traditional numerical and analytical techniques.

---

\*patrick.egenlauf@simtech.uni-stuttgart.de

# 1 Introduction

The exploration of quantum many-body systems far from equilibrium has become a central theme across ultracold-atom physics, condensed-matter theory, and ultrafast spectroscopy. Rapid experimental progress now enables the precise control of isolated atomic gases [1], the manipulation of correlated solids with intense light fields [2, 3], the tracking of real-time electronic motion in nanostructures [4] and much more [5–11]. These advances have revealed a broad spectrum of out-of-equilibrium phenomena (for recent reviews see e.g. [12–14]), including ultrafast switches of currents in dielectrics [15–18], laser-induced superconductivity [2, 10, 19], and ultrafast switches to hidden quantum states [5]. Parallel developments in non-equilibrium many-body theory [16, 20–32] have highlighted the need for theoretical frameworks that faithfully model (strongly) correlated dynamics of extended systems for long periods of time while remaining computationally tractable.

Accurately describing the non-equilibrium dynamics of interacting quantum many-body systems remains a central challenge because the full many-body wave function resides in a Hilbert space whose dimension grows exponentially with the particle number. Wave-function-based methods, which allow a full parametrization of the Hilbert space such as the multiconfigurational time-dependent Hartree Fock method (MCTDHF) [6, 23] or matrix-product-state (MPS) techniques [33–36] provide numerically exact results but are limited to modest system sizes and short propagation times. Other approaches such as the time-dependent density-functional theory (TDDFT) [37, 38] or time-dependent Hartree–Fock (TDHF) [6] scale favorably yet are limited to weakly (TDDFT) or uncorrelated (TDHF) systems. Several approaches exist that avoid the exponential scaling of wavefunctions by using a reduced object instead. One prominent example are methods that use non-equilibrium Green’s functions (NEGF) as the central object (for a review see e.g. [39]). However, NEGF methods typically feature a nonlinear scaling with time. The TD2RDM formalism [31, 32, 40] follows a similar spirit but features a linear scaling in time: the 2RDM  $D_{12}(t)$  contains the exact two-particle information, and the total energy can be expressed as a functional of  $D_{12}(t)$  (if the Hamiltonian only contains one- and two-body operators), thereby reducing the computational cost from exponential to polynomial scaling. Its power stems from the explicit inclusion of dynamical two-particle correlations and from a systematic closure of the BBGKY hierarchy via a reconstruction of the three-particle reduced density matrix (3RDM)  $D_{123}(t)$  as a functional of  $D_{12}(t)$ . The method thus relies on approximate reconstruction functionals; present state-of-the-art schemes are time-local, which guarantees the linear scaling in time of the method, and quadratic in the two-particle cumulant  $\Delta_{12}(t)$ , thereby neglecting memory effects and higher-order cumulants. Consequently, the accuracy of TD2RDM depends on the quality of the time-local  $D_{123}$  reconstruction. We would like to point out that extensions of NEGFs methods featuring a linear scaling in time [27, 28, 30] face the same problem of the necessity to reconstruct unknown components of the equations of motion in a time-local fashion. So, the deep question is, in which regimes can we find a sufficiently accurate time-local reconstruction functional? Can numerical methods shed light on this problem?

Today, machine learning (ML) introduces a diverse variety of complementary approaches to classical numerical modeling. Some approaches can enable integrating domain knowledge about physical laws governing the target problems of interest. In the field of quantum physics, some examples in the existing literature model open quantum systems [41–46], investigate quantum-information tasks [45, 47], measure entanglement [48], use neural quantum states to overcome the exponential scaling in the Hilbert space [49], combine ML with quantum computing [50], and enable quantum (optimal) control [51, 52].

Dynamical processes are generally governed by differential equations and have been subject to numerous investigations using ML [53–68]. In the present study, we focus specifically on systems whose time evolution can be described by ODEs. Neural ODEs offer a powerful venue of thinking

because they combine a rudimentary simulation of propagation of time through a differential equation, with data-driven ML [69]. It is a promising candidate for modeling diverse time-dependent datasets in and out of science [70–77]. To our knowledge, its application in classical or quantum many-body physics is scarce. Neural ODEs have been applied to reduced representations of quantum dynamics [78], holographic quantum chromodynamics [79], or to the Hamiltonian learning problem [80]. Other ML approaches have been used to investigate Markovian and non-Markovian dynamics of quantum systems [81].

Up to now, it is an open question whether neural ODEs will be useful tools to capture complex high-dimensional dynamics of many-body systems, specifically those out of equilibrium. What are the obstacles of established many-body simulations that can be overcome by neural ODEs? Can they supersede performance? Moreover, how can one infuse prior knowledge of, e.g., symmetries and conserved quantities into specifically these ML models, and does this actually lead to improved model fidelity? This might not be straightforward for generic dynamical processes. Finally, can we interpret [82] or extract new knowledge about the target (here, the dynamical quantum system) with ML-based ‘simulation’?

In this paper, we embark on a study of quantum many-body systems out of equilibrium, viewed through 2RDMs [40]. For this purpose, we investigate the dynamics of the paradigmatic Fermi-Hubbard model [83]. Depending on the parameters, it shows a broad range of dynamics, reaching from weakly to strongly correlated. We demonstrate that neural ODEs offer interesting insights: We find indications that time-local reconstructions of the 3RDM may only be possible in certain regimes in the parameter space. The infusion of physics knowledge is neither straightforward nor does prior physical information necessarily lead to better results.

The structure of the paper is as follows: In Sec. 2 we briefly introduce the quenched Fermi-Hubbard model, which will be the system under investigation. We describe the equations of motion for the 2RDM and concisely revisit the cumulant reconstruction needed to close them. The neural ODE model used in this investigation is presented together with the data preprocessing. In Sec. 3, we first identify some structure in the parameter space of the Fermi-Hubbard model. This is used to investigate the performance of the neural ODE across the parameter plane. To improve the stability of the prediction, we enforce physical constraints in the loss. Last, we discuss the results and show perspectives for future investigations in Sec. 4.

## 2 Methods

### 2.1 Non-equilibrium Fermi-Hubbard model

We consider a one-dimensional Fermi-Hubbard chain comprising  $M_s$  physical sites together with two auxiliary sites labeled 0 and  $M_s + 1$  that are fixed to be unoccupied throughout the dynamics. Dirichlet boundary conditions are imposed at these auxiliary sites, a choice that mirrors the confinement used in quantum-simulator experiments with trapped ultracold atoms (see, e.g., Ref. [84]). While Dirichlet boundaries are natural for the experimental setting, alternative boundary conditions (e.g., periodic) can be incorporated straightforwardly within the same formalism. The initial state is prepared in a harmonic trapping potential, which is abruptly switched off at  $t = 0$ , after which the system evolves under the standard Fermi-Hubbard Hamiltonian [40]. The full Hamiltonian in second quantization is given by

$$\mathcal{H} = -J \sum_{\langle i,j \rangle} \sum_{\sigma} a_{i\sigma}^{\dagger} a_{j\sigma} + U \sum_i n_i^{\uparrow} n_i^{\downarrow} + \sum_{i,\sigma} V_i(t) a_{i\sigma}^{\dagger} a_{i\sigma}. \quad (1)$$

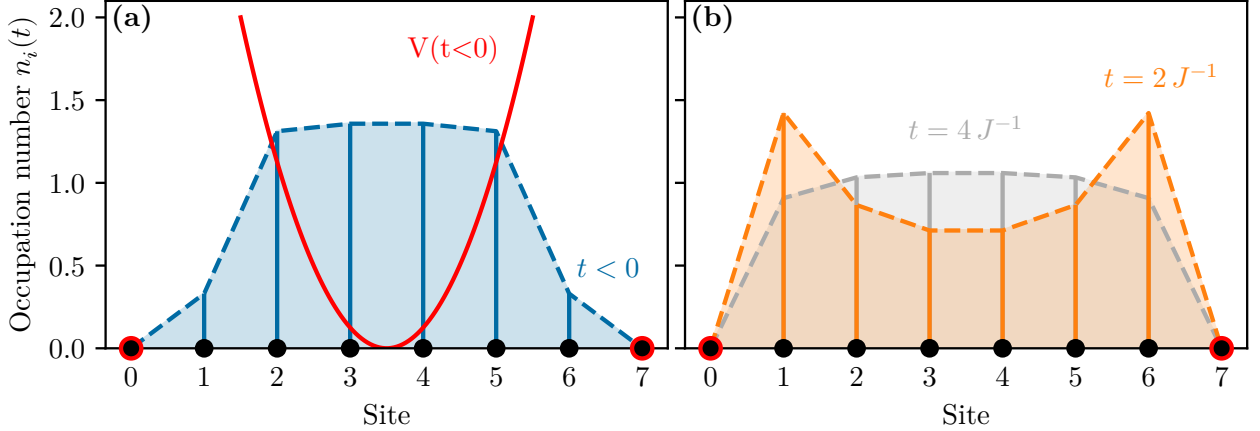


Figure 1: Fermi-Hubbard model consisting of 6 sites, initially ( $t < 0$ ) subject to an external harmonic trap. Dirichlet (hard-wall) boundary conditions on site 0 and 7 are indicated by red circles. (a) The one-particle site-occupation numbers  $n_i$  of the trapped ground state, which correspond to an excited configuration of the unconfined system after the quench. (b) Temporal evolution of the occupations  $n_i(t)$  after the quench, displayed at  $t = 2 J^{-1}$  and  $t = 4 J^{-1}$ . The parameters of Eq. (1) are  $V = J$  and  $U = J$ .

Here,  $J$  denotes the hopping amplitude,  $\langle i, j \rangle$  indicates nearest-neighbor pairs,  $a_{i\sigma}^{(\dagger)}$  are the single-particle annihilation (creation) operators,  $n_i^{\uparrow(\downarrow)} = a_{i\uparrow(\downarrow)}^{\dagger} a_{i\uparrow(\downarrow)}$  are the corresponding spin-resolved occupation number operators at site  $i$ , and  $U$  characterizes the on-site interaction strength governing the correlation energy of the. The system before and after the quench can be seen in Fig. 1.

We use a harmonic potential

$$V_i(t) = \theta(-t) \frac{V^2}{2} \left( i - \frac{M_s + 1}{2} \right)^2, \quad (2)$$

which initially traps the system in the ground state of the harmonic trap and is turned off at  $t = 0$ . This potential quench induces the dynamics. Although this is a quite simple model, it is still complex enough to show rich dynamics.

In the following analysis, we study the spin-symmetric Fermi–Hubbard model at half filling, i.e., with a total particle number  $N = M_s$  and equal numbers of up- and down-spin particles  $N_\uparrow = N_\downarrow$ , corresponding to a total spin-singlet configuration.

## 2.2 Time-evolution of the 2RDM

The 2RDM is defined from the  $N$ -body state  $|\Psi(t)\rangle$  as a trace over all but two particles

$$D_{12}(t) = N(N-1) \text{Tr}_{3\dots N} |\Psi(t)\rangle \langle \Psi(t)| \quad (3)$$

with  $N(N-1)$  being the chosen normalization. The second equation in the BBGKY hierarchy, i.e., the equation of motion for the 2RDM,

$$i\partial_t D_{12} = [h_1 + h_2 + W_{12}, D_{12}] + \text{Tr}[W_{13} + W_{23}, D_{123}], \quad (4)$$

contains the single-particle Hamiltonian  $h_i$ , the two-body interaction  $W_{ij}$ , and the 3RDM  $D_{123}$ . Closing Eq. (4) therefore requires a reconstruction functional  $D_{123}^R[D_{12}]$ . This leads to the TD2RDM theory introduced in Refs. [31, 32, 40].

In a total-spin-singlet configuration, as considered here, the evaluation of Eq. (4) requires only the mixed-spin block  $\langle j_1 \uparrow j_2 \downarrow | D_{12}(t) | i_1 \uparrow i_2 \downarrow \rangle = D_{i_1 \uparrow i_2 \downarrow}^{j_1 \uparrow j_2 \downarrow}(t)$  with  $|i_1 \uparrow i_2 \downarrow\rangle$  two-particle product states of spin orbitals, which already encodes the complete information of the full 2RDM  $D_{12}(t)$  [31]. For completeness we note that elements of the 2RDM can also be obtained in the second quantization formalism through  $D_{i_1 \uparrow i_2 \downarrow}^{j_1 \uparrow j_2 \downarrow}(t) = \langle \Psi(t) | a_{i_1 \uparrow}^\dagger a_{i_2 \downarrow}^\dagger a_{j_2 \downarrow} a_{j_1 \uparrow} | \Psi(t) \rangle$ . All other spin components can be recovered from this block by straightforward exchange or spin-flip symmetry relations.

### 2.2.1 Cumulant expansion

Any  $p$ RDM can be decomposed into antisymmetrised products of lower-order RDMs plus a connected part (the cumulant) [85]. For the 2RDM the decomposition reads

$$D_{12} = \hat{A}D_1D_2 + \Delta_{12}, \quad (5)$$

where  $\hat{A}$  antisymmetrises the product and  $\Delta_{12}^{(2)}$  is the two-particle cumulant. For the 3RDM one obtains

$$D_{123} = \hat{A}D_1D_2D_3 + \hat{A}\Delta_{12}D_3 + \Delta_{123}, \quad (6)$$

where  $D_{123}$  is the three-particle cumulant (the genuinely connected three-body correlation). We have chosen a convention for  $\hat{A}$  such that every topologically distinct term contributes only ones in order to avoid normalization in the cumulant expansion Eq. (6). The first term contains only products of the 1RDM so that the three particles are uncorrelated in their dynamics. The second term shows that once the two-particle cumulant  $\Delta_{12}$  is known, all pairwise correlations in the three-body system are already determined; only the last term  $\Delta_{123}$  adds the correlated three-body part. As has been shown in Ref. [31], parts of the three-particle cumulant  $\Delta_{123}$  can be exactly reconstructed from the 2RDM through the knowledge of its traces. The irreducible three-body part of  $\Delta_{123}$  denoted as  $\Delta_{123,K}$  with  $\text{Tr}_3\Delta_{123,K} = 0$ , however, cannot be expressed through lower-order RDMs. Consequently, an accurate reconstruction of  $D_{123}$  depends on a good approximation of  $\Delta_{123,K}$ , while the bulk of the many-body information is already encoded in  $D_{12}$  (through  $\Delta_{12}$ ).

All practical TD2RDM implementations close the BBGKY hierarchy by replacing the 3RDM  $D_{123}$  with a functional of the 2RDM  $D_{12}$  (i.e. of the two-particle cumulant  $\Delta_{12}$ ). The most widely employed approximations are time-local, thereby neglecting any memory dependence. A more detailed derivation and specific functional forms can be found in Ref. [40].

### 2.3 Neural ODE

Neural ODEs provide a data-driven framework to learn a continuous-time dynamical system from sampled trajectories [69]. Given a set of discrete 2RDM snapshots  $\{D_{i_1 \uparrow i_2 \downarrow}^{j_1 \uparrow j_2 \downarrow}(t_k)\}_{k=0}^K$  obtained from the propagation of the wavefunction through exact diagonalization of the Schrödinger equation, a neural ODE seeks a parametric vector field  $\mathcal{F}_\theta(D_{i_1 \uparrow i_2 \downarrow}^{j_1 \uparrow j_2 \downarrow})$  such that

$$\frac{d}{dt} D_{i_1 \uparrow i_2 \downarrow}^{j_1 \uparrow j_2 \downarrow}(t) = \mathcal{F}_\theta(D_{i_1 \uparrow i_2 \downarrow}^{j_1 \uparrow j_2 \downarrow}(t)), \quad (7)$$

where  $\theta$  denotes the trainable network parameters. The loss function is the integrated discrepancy between the network prediction and the reference data,

$$\mathcal{L}(\theta) = \frac{1}{K} \sum_{k=1}^K \|\Phi_\theta(t_k; D_{i_1 \uparrow i_2 \downarrow}^{j_1 \uparrow j_2 \downarrow}(t_0)) - D_{i_1 \uparrow i_2 \downarrow}^{j_1 \uparrow j_2 \downarrow}(t_k)\|_F^2, \quad (8)$$

with  $\Phi_\theta$  the solution of the neural ODE obtained by an adaptive ODE solver and  $\|\cdot\|_F$  the Frobenius (Schatten-2) norm. After training, the learned vector field can be evaluated on unseen initial conditions to test whether the dynamics is well described by a time-local functional of the instantaneous 2RDM.

Thus, neural ODEs serve as an independent, model-agnostic diagnostic tool to map the parameter regimes (in the  $U$ - $V$  plane) where the TD2RDM closure can be reliably approximated by time-local reconstructions as discussed in Sec. 2.2.1.

In practice, we employ a fully connected architecture with two hidden layers, each with a dimension of 2048. The mixed-spin block of the 2RDM  $D_{i_1 i_2}^{j_1 \uparrow j_2 \downarrow}$  contains 1296 complex-valued entries. To pass them through the neural ODE, we must separate the real and imaginary parts, yielding a total of 2592 real values. This can be reduced by leveraging its hermeticity and taking only the upper triangular values, which in turn results in 1296 real values. For each parameter configuration in the  $U$ - $V$  plane, we divide our time series into training, validation, and test sets. The first 3000 time steps are used for training and the next 1000 time steps are used for validation, where one time step is  $\Delta t = 0.01 J^{-1}$ . The remainder can be used for testing. We apply min-max normalization to the real and imaginary parts separately to scale them to  $[0, 1]$ . Here, we first normalize the train set, then use the same normalization constants for both the validation and test sets. We use the Python library `torchdiffeq` [86] for the implementation of the neural ODE.

It is important to mention that, compared to other applications of neural ODEs, which typically reduce high-dimensional data to a lower-dimensional manifold and then train the neural ODE on the low-dimensional representation [74, 87–90], we train the model directly on the high-dimensional data. Furthermore, the size of the training set is of the same order of magnitude as the dimensionality. To our best knowledge, this is the first time that neural ODEs has been trained in this way, which, if successful, could open up new application possibilities.

## 3 Results

### 3.1 Time-local reconstruction for different parameter configurations

To determine where a time-local reconstruction of the three-particle cumulant  $\Delta_{123}(t)$  is justified, we first analyze three quantitative indicators obtained from the exact dynamics of the two- and the kernel component of the three-particle cumulants,  $\Delta_{12}(t)$  and  $\Delta_{123,K}(t)$ , for a broad range of interaction strengths  $U$  and quench amplitudes  $V$ . These measures serve both to interpret the neural ODE results and to determine the general structure of the  $U$ - $V$  parameter plane.

The net increase of genuine three-particle correlations in the irreducible component during the evolution is quantified by

$$\overline{\delta\Delta_{123,K}^{\uparrow\downarrow\downarrow}} = \frac{1}{T} \int_0^T \left\| \Delta_{123,K}^{\uparrow\downarrow\downarrow}(t) \right\| - \left\| \Delta_{123,K}^{\uparrow\downarrow\downarrow}(0) \right\| dt, \quad (9)$$

where  $\|\cdot\|$  denotes the Frobenius norm. The contour  $\delta\Delta_{123,K} = 0.65$  separates regimes of moderate ( $\delta\Delta_{123,K} \leq 0.65$ ) and strong ( $\delta\Delta_{123,K} > 0.65$ ) three-particle correlations buildup, as visible in Fig. 2(a). This choice is empirical as it delimits the regimes very well. All three quantities are evaluated for  $T = 50 J^{-1}$  for the whole parameter scan.

The instantaneous two-particle correlation energy is defined as

$$E_{\text{corr}}(t) = \text{Tr}_{12} W_{12} \Delta_{12}(t), \quad (10)$$

which in the case of the Fermi-Hubbard model reduces to

$$E_{\text{corr}}(t) = U \sum_j \Delta_{j\uparrow j\downarrow}^{j\uparrow j\downarrow}(t). \quad (11)$$

We compare the time-averaged correlation energy

$$\bar{E}_{\text{corr}} = \frac{1}{T} \int_0^T E_{\text{corr}}(t) dt, \quad (12)$$

with the initial potential energy of the quenched state

$$E_{\text{pot}}(0) = \text{Tr } D_1(t=0) V_1(t=0) \quad (13)$$

in Fig. 2(b). The colour scale is truncated at  $-0.1$  for visual clarity; values below this threshold are present but not displayed. Throughout the explored parameter space, the correlation energy is initially negative and increases during the time evolution, attaining positive average values for some parameter configurations. Figure 2(b) thus visualizes the buildup of two-particle correlations. The cut-off at  $-0.1$  was chosen empirically to separate regimes of pronounced correlation-energy increase from those exhibiting only a modest rise. Both contour lines in Fig. 2 indicate structures in the dynamics of the 2RDM across the parameter plane, which serve as reference lines for better comparability across plots.

We hypothesize that in regions with high (anti-)correlation between two-particle and three-particle cumulants, the neural ODE should perform well: The information about the three-particle cumulant, which is required to close the equations of motion for the 2RDM, should be contained in the 2RDM. In the anti-correlated regime, there is a strong correlation between these two quantities, though negative. This could hint at the existence of a time-local reconstruction functional in the anti-correlated regime since the current reconstructions only perform well in the positively correlated regime. The existence of such a functional would allow efficient numerical integration of the equations of motion with accurate results in this regime. The neural ODE serves as a model-agnostic tool: It can only learn Markovian dynamics by design. Thus, if memory is required to reconstruct the three-particle cumulant and hence close the equations of motion, the model should not be able to learn and predict the exact dynamics of the 2RDM.

To assess this hypothesis, we look at the Pearson correlation coefficient  $C_{f,g}$  [91], which provides a quantitative measure of the linear relationship between two time-dependent observables  $f(t)$  and  $g(t)$ . It is defined as the normalized covariance

$$C_{f,g} = \frac{\frac{1}{T-t_0} \int_{t_0}^T [f(t) - \bar{f}] [g(t) - \bar{g}] dt}{\sigma_f \sigma_g}, \quad (14)$$

where  $\bar{f}$  and  $\bar{g}$  denote the temporal averages

$$\bar{f} = \frac{1}{T-t_0} \int_{t_0}^T f(t) dt, \quad \bar{g} = \frac{1}{T-t_0} \int_{t_0}^T g(t) dt, \quad (15)$$

and  $\sigma_f, \sigma_g$  are the corresponding standard deviations

$$\sigma_f = \sqrt{\frac{1}{T-t_0} \int_{t_0}^T [f(t) - \bar{f}]^2 dt}, \quad \sigma_g = \sqrt{\frac{1}{T-t_0} \int_{t_0}^T [g(t) - \bar{g}]^2 dt}. \quad (16)$$

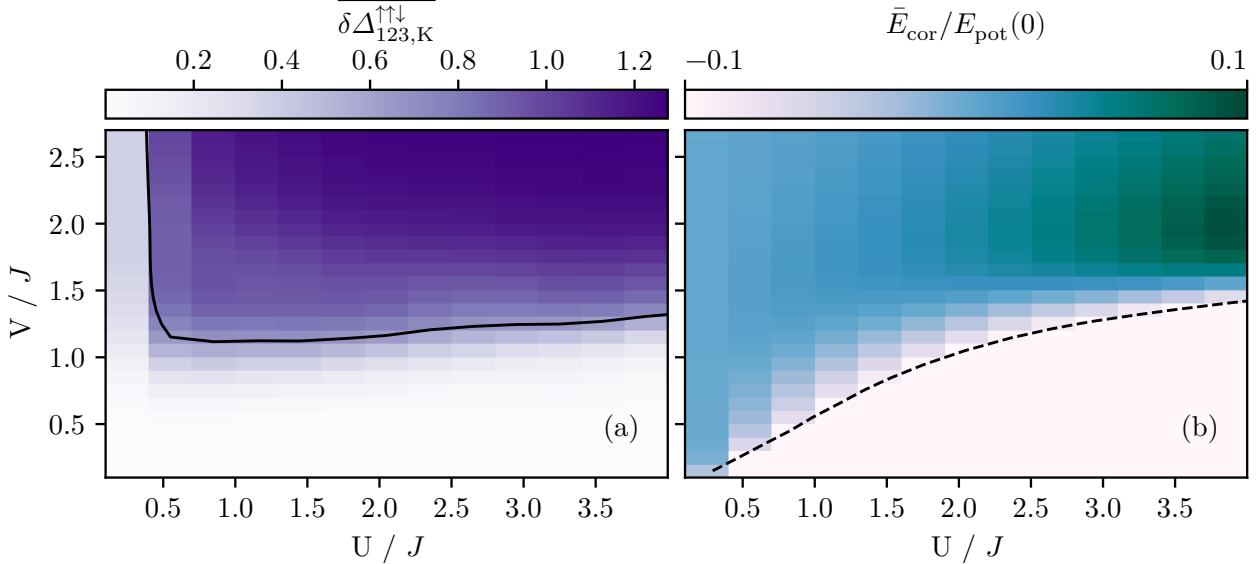


Figure 2: We study the six-site Fermi-Hubbard model of Eq. (1). Both plots show a parameter scan over the initial potential strength  $V$  and the interaction  $U$ . The dynamical buildup of three-particle correlations as described in Eq. (9) is visualized in (a). The solid black line corresponds to  $\delta\Delta_{123,K}^{\uparrow\uparrow} = 0.65$ , which indicates the crossover between moderate and strong correlation buildup. In (b) the time-averaged correlation energy relative to the initial excitation energy  $\bar{E}_{\text{corr}}/E_{\text{pot}}(0)$  is shown, where the black dashed line corresponds to  $\bar{E}_{\text{corr}}/E_{\text{pot}}(0) = -0.1$ . This delimits the regime of strong two-particle correlation buildup. Both values were chosen in accordance with Fig. 3 since they also delimit the positive and negative as well as the strong and weak correlations of the cumulant dynamics, respectively.

By construction,  $-1 \leq C_{f,g} \leq 1$ ;  $C_{f,g} = 1$  ( $-1$ ) indicates perfect (anti-)correlation, while  $C_{f,g} = 0$  corresponds to the absence of linear correlation. In the present work,  $C_{f,g}$  is employed to assess the temporal correlation between the two-particle cumulant  $\Delta_{12}(t)$  and the kernel component of the three-particle cumulant  $\Delta_{123,K}(t)$ . Since the initial rise of the cumulants is always correlated and we are only interested in the correlations of the steady-state fluctuations, we omit the start of the time series and empirically choose  $t_0 = 10 J^{-1}$ . According to our hypothesis, a high absolute value of  $C_{\Delta_{12},\Delta_{123,K}}$  supports the validity of time-local reconstruction functionals, whereas low absolute values signal the need for memory-dependent extensions. In Fig. 3(a) and (b) the Pearson correlation coefficient between the kernel component of the three-particle cumulant  $\Delta_{123,K}^{\uparrow\uparrow}$  and the two-particle cumulants  $\Delta_{12}^{\uparrow\uparrow}$  and  $\Delta_{12}^{\uparrow\downarrow}$ , respectively, are shown. Both contour lines, which are equal to those in Fig. 2, indicate the crossover between positive and negative correlation ( $\delta\Delta_{123,K}^{\uparrow\uparrow} = 0.65$ ), and to the region of strong time correlation ( $\bar{E}_{\text{corr}}/E_{\text{pot}}(0) = -0.1$ ). Note that evaluating in Fig. 2 and 3 the entire three-particle cumulant instead of only the kernel component (such as in Ref. [40]) leads to almost the same results because the trace information is a small, practically time-independent contribution.

We use  $D_{12}(t_0 = 40 J^{-1})$  as the initial input to the neural ODE, which is then employed to predict the subsequent evolution of the 2RDM starting from  $t_0 = 40 J^{-1}$ . Consequently, we define the prediction length as

$$t_{\text{pred}} = t - t_0. \quad (17)$$

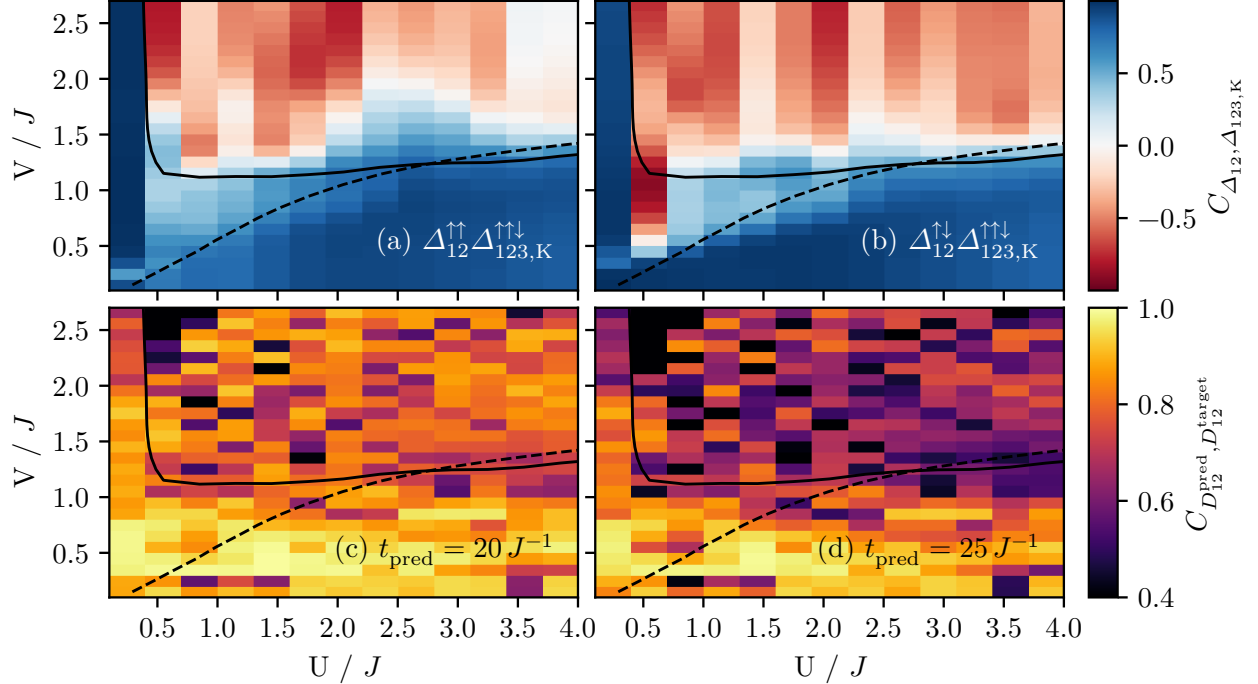


Figure 3: In (a) and (b) the Pearson correlation coefficient  $C_{\Delta_{12}, \Delta_{123,K}}$  between the kernel component of the three-particle cumulant  $\Delta_{123,K}^{\uparrow\uparrow\downarrow}$  and the two-particle cumulants  $\Delta_{12}^{\uparrow\uparrow}$  and  $\Delta_{12}^{\uparrow\downarrow}$  are shown, respectively, across the  $U$ - $V$  plane for the six-site Fermi-Hubbard model of Eq. (1). The contour lines  $\delta\Delta_{123,K}^{\uparrow\uparrow\downarrow} = 0.65$  and  $\bar{E}_{\text{corr}}/E_{\text{pot}}(0) = -0.1$  from Fig. 2 are visualized as well. In (c) and (d) the Pearson correlation coefficient between the predicted and the exact time series of the 2RDM  $C_{D_{12}^{\text{pred}}, D_{12}^{\text{target}}}$  is visualized for a prediction length of  $t_{\text{pred}} = 20 J^{-1}$  and  $t_{\text{pred}} = 25 J^{-1}$  (2000 and 2500 time steps), respectively, starting from  $D_{12}(t = 40 J^{-1})$ . For each parameter configuration, one model was trained.

To quantify the predictive performance of the neural ODE, we calculate the Pearson correlation coefficient between the predicted time series of the 2RDM and the actual time series for the reduced representation (upper triangular values only)  $C_{D_{12}^{\text{pred}}, D_{12}^{\text{target}}}$  for a prediction length of  $t_{\text{pred}} = 20 J^{-1}$  and  $t_{\text{pred}} = 25 J^{-1}$  (2000 and 2500 time steps) starting from  $D_{12}(t = 40 J^{-1})$ , visualized in Fig. 3(c) and (d), respectively. The contour lines are the same as in Fig. 2. For a prediction length of  $t_{\text{pred}} = 20 J^{-1}$  the performance is high in the correlated regime and reasonably good in the anti-correlated regime. However, for a longer prediction length of  $t_{\text{pred}} = 25 J^{-1}$ , the performance in the anti-correlated regime drops significantly, while it remains good in the correlated regime.

To further investigate the accuracy of the prediction, we calculate two quantities from the predicted time series, namely the occupation number  $n(t)$  and the doublon occupation number  $d(t)$  (number of pairs on a site). Since all sites show similar dynamics, we only consider site 1. The accuracy of the prediction is determined by the time-integrated deviations from the exact result

$$\frac{\delta n_1}{\overline{n_1}} = \frac{\frac{1}{T} \int_{t_0}^{t_0+T} |n_1^{\text{target}}(t) - n_1^{\text{predicted}}(t)| dt}{\frac{1}{T} \int_{t_0}^{t_0+T} n_1^{\text{target}}(t) dt}. \quad (18)$$

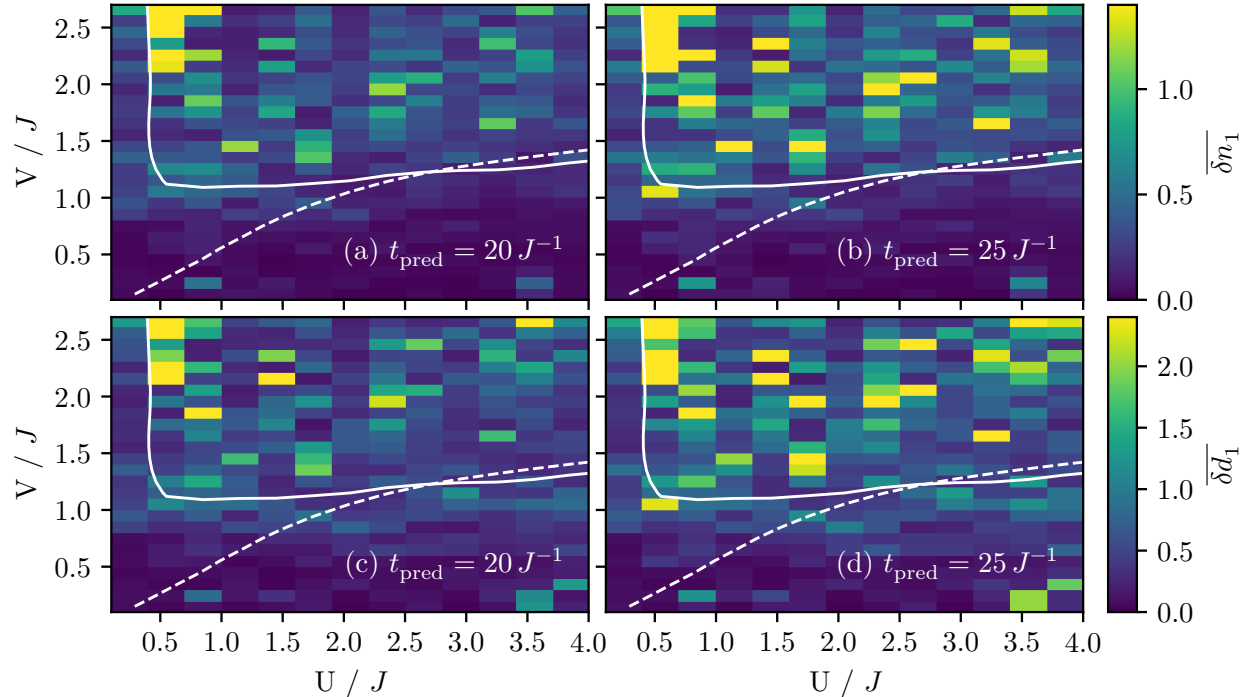


Figure 4: The upper plots show the time-integrated deviations of the occupation number of site 1 as described in Eq. (18) between the predicted and the exact occupation number over time for a prediction length of (a)  $t_{\text{pred}} = 20 J^{-1}$  and (b)  $t_{\text{pred}} = 25 J^{-1}$ . Similarly, in (c) and (d) the same quantity is illustrated for the doublon occupation number  $d_1$  of site 1. The contour lines  $\delta\Delta_{123,K}^{\uparrow\uparrow} = 0.65$  and  $\bar{E}_{\text{corr}}/E_{\text{pot}}(0) = -0.1$  from Fig. 2 are visualized as well. For each parameter configuration, one model was trained, with the prediction starting from  $D_{12}(t = 40 J^{-1})$ .

This quantity as well as the deviations for the doublon occupation number  $\bar{\delta d_1}$  are shown in Fig. 4 for both prediction lengths. Again, we can see that the error is low in the correlated regime, while it is high in the anti-correlated regime. Figure 4 also depicts that even for a shorter prediction length, there is a significant difference in the accuracy of the prediction in the correlated and anti-correlated regimes.

These results contradict our hypothesis and thus suggest that there might be no time-local reconstruction functional in the anti-correlated regime. The solid contour line separates moderate from strong correlations buildup of the kernel component of the three-particle cumulant ( $\delta\Delta_{123,K}^{\uparrow\uparrow} = 0.65$ ). In both Fig. 3 and 4, this line quite accurately localizes regions of good and bad performance, indicating that the existence of a time-local reconstruction functional depends on this quantity.

Training one model for one parameter configuration in the  $U$ - $V$  plane took approximately 6 hours on an NVIDIA A100 GPU. Due to the high computational cost and the huge amount of parameter configurations, we were able to train only one model per configuration. This explains the fluctuations in the performance across the  $U$ - $V$  plane in Fig. 3 and 4, which could be reduced by either training an ensemble of models or performing hyper-parameter optimization for each parameter configuration. Even though these fluctuations exist, the trends in performance in the different regimes described above are clearly discernible.

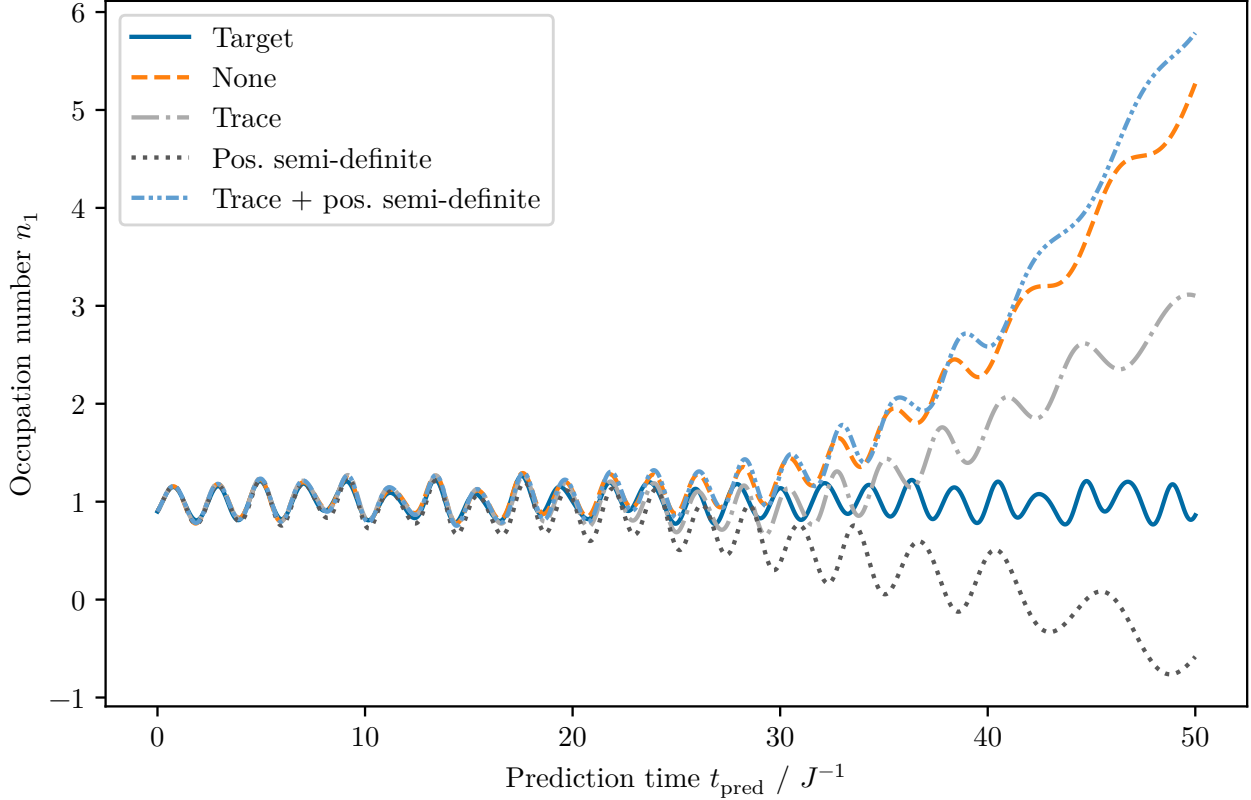


Figure 5: The occupation number  $n_1$  of site 1 of the six-site Fermi-Hubbard model described in Eq. (1), with  $V = 1.0$  and  $U = 3.1$ , is visualized over time by the blue solid line. The occupation number is calculated from the 2RDM. The predicted occupation number of four hyper-parameter optimized models trained on different losses are shown as well, all trained on the first 3000 time steps ( $30 J^{-1}$ ) of the time series. The orange dashed line was trained on the MSE loss only, the light gray dash-dotted line additionally on the constraint loss for the trace  $\mathcal{L}_{\text{tr}}$ , and the dark gray dotted line on the MSE and the negative eigenvalue loss  $\mathcal{L}_{\text{psd}}$ . The prediction starts from  $D_{12}(t = 40 J^{-1})$ , hence this is an extrapolation.

### 3.2 Stability of the prediction

In the previous section, we focused on the short- to medium-term forecast. In Fig. 5, we consider the long-term prediction. The prediction diverges after a prediction time of about  $t_{\text{pred}} = 25 - 30 J^{-1}$ . Interestingly, the same behavior is observed in the analytical TD2RDM theory [40]. To stabilize the TD2RDM method, several necessary  $N$ -representability conditions are enforced during integration by means of a purification procedure [40, 92–95]. Specifically, the positive semi-definiteness of the 2RDM and the two-hole reduced density matrix (2HRDM) are imposed. The matrix elements of the 2HRDM  $Q_{12}(t)$  are given by  $Q_{i_1\uparrow i_2\downarrow}^{j_1\uparrow j_2\downarrow} = \langle \Psi(t) | a_{j_1\uparrow} a_{j_2\downarrow} a_{i_1\uparrow}^\dagger a_{i_2\downarrow}^\dagger | \Psi(t) \rangle$ . Empirically, it has been found that this purification procedure stabilizes the TD2RDM very well in all parameter regions, where the time-local reconstruction functionals produce a sufficiently small error in the overall propagation [95].

The question arises whether we can enforce these conditions on the neural ODE as well? Do they stabilize the model's long-term predictions? How do they perform compared to the unconstrained model? To enforce constraints in ML, there are, in principle, two options: i) weak constraints

enforce the conditions via the loss function during training, while ii) hard constraints are built into the architecture of the model itself, preventing the model from violating these constraints. In the following, we will focus on weak constraints and their results.

### 3.2.1 Weak constraints

The weak constraints are enforced via the loss function

$$\mathcal{L} = \text{MSE}(\hat{y}, y) + \sum_i \alpha_i \mathcal{L}_{\text{constraint},i}, \quad (19)$$

with the mean square error as standard loss and the different constraints  $\mathcal{L}_{\text{constraint},i}$  scaled with a factor  $\alpha_i$ .

Due to their positive semi-definiteness, the negative eigenvalues  $\lambda_j^t$  for both the 2RDM  $D_{12}(t)$  and the 2HRDM  $Q_{12}(t)$  at time  $t$  are penalized via

$$\mathcal{L}_{\text{psd}} = \frac{1}{T} \sum_{t=0}^T \sum_j \text{ReLU}(-\lambda_j^t)^2. \quad (20)$$

The rectified linear unit (ReLU) is squared to obtain a continuous derivative. Thus, we have two additional terms in the loss, one for the 2RDM and one for the 2HRDM. Similary, the trace conservation of the 2RDM over time

$$\sum_n \sum_m D_{n\uparrow m\downarrow}^{n\uparrow m\downarrow}(t) = N_{\uparrow} N_{\downarrow} = 9, \quad \forall t \quad (21)$$

is enforced through the loss

$$\mathcal{L}_{\text{tr}} = \frac{1}{T} \sum_{t=0}^T \left( \sum_n \sum_m D_{n\uparrow m\downarrow}^{n\uparrow m\downarrow}(t) - 9 \right)^2 \quad (22)$$

for the 2RDM  $D_{12}(t)$  and analogously for the 2HRDM  $Q_{12}(t)$ .

For the following analysis, we focus on the parameter configuration  $V = 1.0 J$  and  $U = 3.1 J$  because of its dynamics, which is neither too slow nor too fast. Additionally, it is in the correlated regime, where the prediction should, in principle, work, but the performance in Fig. 3(d) is not perfect yet ( $C_{D_{12}^{\text{pred}}, D_{12}^{\text{target}}} = 0.6899$ ). First, we optimize the model's hyperparameters, resulting in much better performance:  $C_{D_{12}^{\text{pred}}, D_{12}^{\text{target}}} = 0.9194$ . This supports the previous statement that the fluctuations in the performance in Fig. 3(c) and (d) could be reduced by hyper-parameter optimization. Next, we train three models on different combinations of the constraints, one on the trace constraint only, one on the eigenvalue constraint only, and one on both. Again, we optimize the hyperparameters of each model for a fair comparison. As depicted in Fig. 5, these constraints do not stabilize the long-term prediction. In fact, they all start to diverge at a similar prediction length, as defined in Eq. (17),  $25 J^{-1} < t_{\text{pred}} < 30 J^{-1}$ . In Fig. 6 the Pearson correlation coefficient  $C_{D_{12}^{\text{pred}}, D_{12}^{\text{target}}}$  and the different loss terms over the length of the prediction are visualized. The same divergent behavior is observed in the Pearson correlation. All models show similar performance across the various loss metrics, except for trace loss, where models trained with this constraint perform about two orders of magnitude better. However, this only leads to a minimally longer stable forecast length in the case of the trace constraint model, while there is no improvement for the model trained with both constraints. In general, the losses for the 2RDM are lower than

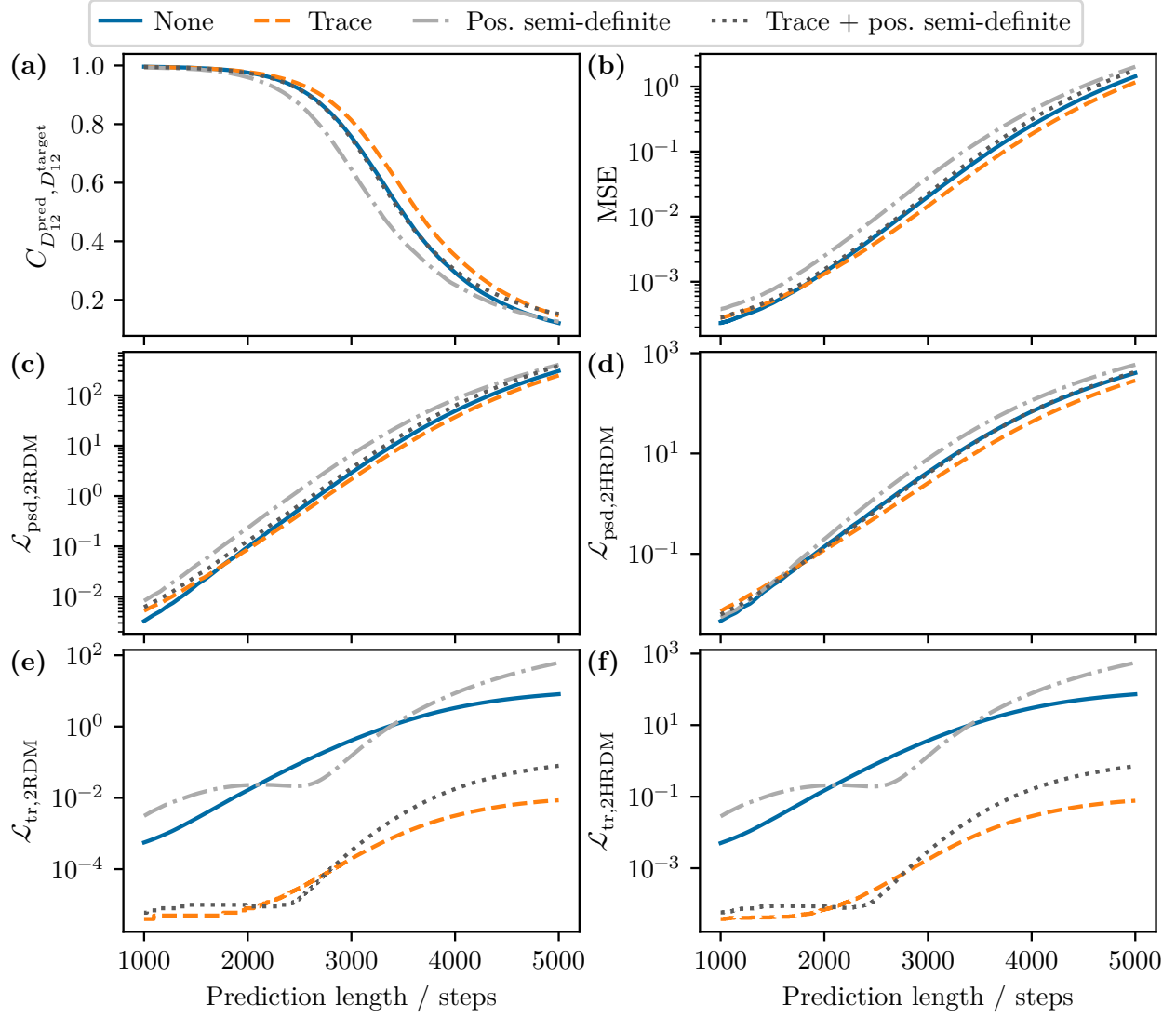


Figure 6: The Pearson correlation coefficient  $C_{D_{12}^{\text{pred}}, D_{12}^{\text{target}}}$  (a), the MSE loss (b), the eigenvalue loss for the 2RDM  $\mathcal{L}_{\text{psd},2\text{RDM}}$  (c), and the 2HRDM  $\mathcal{L}_{\text{psd},2\text{HRDM}}$  (d), as well as the trace loss for the 2RDM  $\mathcal{L}_{\text{tr},2\text{RDM}}$  (e) and the 2HRDM  $\mathcal{L}_{\text{tr},2\text{HRDM}}$  (f) for models trained on different losses are all visualized over the length of the prediction. The blue solid line represents the unconstrained model, which was trained only on MSE loss. Models that had either trace constraint or negative eigenvalue constraint as additional loss terms are depicted as an orange dashed line and a light gray dashed-dotted line, respectively. The dark gray dotted line indicates the model trained with all of the previously mentioned loss terms.

those for the 2HRDM, which is to be expected since the model is only trained directly with the 2RDM data, while the 2HRDM is derived from it. Interestingly, for short-term predictions up to a prediction length of  $t_{\text{pred}} = 1700 \text{ steps} = 17 J^{-1}$  the unconstrained model performs best, but only slightly. This can be seen in the loss plots of the MSE and the eigenvalue constraint.

We note that training the constraint models took significantly longer, as the eigenvalues and trace had to be calculated for each time step of the prediction.

## 4 Discussion and Conclusion

Non-equilibrium dynamics in the Fermi-Hubbard model is Markovian on the level of the full many-body Schrödinger equation. Intricate non-Markovian behavior arises upon reduction of degrees of freedom, e.g. see Ref. [41]. Tracing out degrees of freedom from the full wave function leads to reduced density matrices such as the 2RDM. In this work, we showed how the neural ODE serves as a model-agnostic diagnostic tool to identify the degree of Markovianity of the 2RDM  $D_{12}(t)$  dynamics. Its ability to reproduce the exact trajectories without any explicit knowledge about the 3RDM confirms that, in regimes where the Pearson coefficient  $C_{\Delta_{12}, \Delta_{123,K}}$  is large, the dynamics is effectively governed by a time-local functional of the instantaneous two-particle cumulant  $\Delta_{12}(t)$ . This means that no memory is required for the propagation. In the anti-correlated regime, where  $C_{\Delta_{12}, \Delta_{123,K}}$  becomes negative, the neural ODE fails to predict the evolution, indicating that no simple time-local reconstruction of the three-particle cumulant  $\Delta_{123}(t)$  exists. In other words, memory is required.

An analysis of the buildup of genuine three-particle correlations  $\overline{\delta\Delta_{123,K}^{\uparrow\uparrow\downarrow}}$  reveals that the magnitude of  $\overline{\delta\Delta_{123,K}^{\uparrow\uparrow\downarrow}}$  is the primary factor limiting the applicability of current reconstruction functionals. Regions with  $\overline{\delta\Delta_{123,K}^{\uparrow\uparrow\downarrow}} < 0.65$  coincide with accurate neural ODE forecasts and low reconstruction errors, whereas larger values correlate with the breakdown of both the neural ODE and the TD2RDM method.

These observations suggest a natural extension of the neural ODE framework: by endowing the vector field with explicit history dependence – e.g., through finite-time convolutions – one can empirically determine the minimal memory length required for an accurate reconstruction of  $\Delta_{123}(t)$ . Such a memory-aware neural ODE would provide quantitative guidance for developing non-local reconstruction functionals that incorporate the necessary temporal kernels.

During training, we imposed weak physical constraints (norm conservation and positive semi-definiteness) via additional loss terms. Although the norm constraint improves predictions slightly, the constraints did not yield a noticeable enhancement of long-time stability. Enforcing hard constraints is more challenging for neural ODEs because they learn derivatives, thus symmetries that apply on the level of the integrated observable cannot be implemented straightforwardly into the architecture of the model. Recent proposals for constrained neural differential equations as in Ref. [96] offer promising routes to incorporate such hard constraints.

Finally, this study shows that neural ODEs can be trained on high-dimensional data even with few data samples (with dimensionality of the same order as the number of samples in the training set), which, to the authors' knowledge, has not yet been described in literature. Despite the large state space, the learned model provides reliable short- to medium-term predictions (up to  $t_{\text{pred}} \approx 30 J^{-1} = 3000 \text{ steps}$ ) across a broad range of interaction strengths  $U$  and quench amplitudes  $V$ , which opens up new application possibilities.

## Acknowledgments

We thank Katharina Buczolich, Elias Pescoller, Marie Eder, Florian Grüner, Mathias Niepert, Maria Wirzberger, Max Weinmann, and Mario Gaimann for helpful and stimulating discussions. MK and PE are gratefully funded by Deutsche Forschungsgemeinschaft (DFG, German Research Foundation) under Germany’s Excellence Strategy – EXC 2075 – 390740016 and PE by the Ministry of Science, Research and the Arts Baden-Württemberg (Az. 33-7533-9-19/54/5) in “Künstliche Intelligenz & Gesellschaft: Reflecting Intelligent Systems for Diversity, Demography and Democracy” (IRIS3D). We thank the Stuttgart Center for Simulation Science (SimTech) and the Interchange Forum for Reflecting on Intelligent Systems (IRIS) at the University of Stuttgart, the Heidelberg Academy of Sciences and Humanities, and (PE) the International Max Planck Research School for Intelligent Systems (IMPRS-IS) for further support. IB thanks the Austrian Research Fund (FWF) through grant P35539-N for support. Computations have been performed on the Austrian Scientific Cluster (ASC) and the Experimental Compute Cluster: ehlers at the University of Stuttgart.

## References

- [1] C. Kollath, U. Schollwöck, and W. Zwerger. “Spin-Charge Separation in Cold Fermi Gases: A Real Time Analysis”. In: *Phys. Rev. Lett.* 95 (2005), p. 176401. DOI: [10.1103/PhysRevLett.95.176401](https://doi.org/10.1103/PhysRevLett.95.176401).
- [2] M. Buzzi et al. “Higgs-Mediated Optical Amplification in a Nonequilibrium Superconductor”. In: *Phys. Rev. X* 11 (2021), p. 011055. DOI: [10.1103/PhysRevX.11.011055](https://doi.org/10.1103/PhysRevX.11.011055).
- [3] C. Giannetti et al. “Ultrafast optical spectroscopy of strongly correlated materials and high-temperature superconductors: a non-equilibrium approach”. In: *Advances in Physics* 65 (2016), p. 58. DOI: [10.1080/00018732.2016.1194044](https://doi.org/10.1080/00018732.2016.1194044).
- [4] J. A. Driscoll, S. Bubin, and K. Varga. “Laser-induced electron emission from nanostructures: A first-principles study”. In: *Phys. Rev. B* 83 (2011), p. 233405. DOI: [10.1103/PhysRevB.83.233405](https://doi.org/10.1103/PhysRevB.83.233405).
- [5] L. Stojchevska et al. “Ultrafast Switching to a Stable Hidden Quantum State in an Electronic Crystal”. In: *Science* 344 (2014), p. 177. DOI: [10.1126/science.1241591](https://doi.org/10.1126/science.1241591).
- [6] J. Caillat et al. “Correlated multielectron systems in strong laser fields: A multiconfiguration time-dependent Hartree-Fock approach”. In: *Phys. Rev. A* 71 (2005), p. 012712. DOI: [10.1103/PhysRevA.71.012712](https://doi.org/10.1103/PhysRevA.71.012712).
- [7] G. E. Topp et al. “All-Optical Nonequilibrium Pathway to Stabilising Magnetic Weyl Semimetals in Pyrochlore Iridates”. In: *Nature Communications* 9 (2018), p. 4452. DOI: [10.1038/s41467-018-06991-8](https://doi.org/10.1038/s41467-018-06991-8).
- [8] J. Vodeb et al. “Non-Equilibrium Quantum Domain Reconfiguration Dynamics in a Two-Dimensional Electronic Crystal and a Quantum Annealer”. In: *Nature Communications* 15 (2024), p. 4836. DOI: [10.1038/s41467-024-49179-z](https://doi.org/10.1038/s41467-024-49179-z).
- [9] J. Bedow, E. Mascot, and D. K. Morr. “Emergence and Manipulation of Non-Equilibrium Yu-Shiba-Rusinov States”. In: *Communications Physics* 5 (2022), p. 281. DOI: [10.1038/s42005-022-01050-7](https://doi.org/10.1038/s42005-022-01050-7).
- [10] M. Budden et al. “Evidence for Metastable Photo-Induced Superconductivity in K3C60”. In: *Nature Physics* 17 (2021), p. 611. DOI: [10.1038/s41567-020-01148-1](https://doi.org/10.1038/s41567-020-01148-1).

[11] A. Pohl, P.-G. Reinhard, and E. Suraud. “Towards Single-Particle Spectroscopy of Small Metal Clusters”. In: *Phys. Rev. Lett.* 84 (2000), p. 5090. DOI: [10.1103/PhysRevLett.84.5090](https://doi.org/10.1103/PhysRevLett.84.5090).

[12] D. N. Basov, R. D. Averitt, and D. Hsieh. “Towards properties on demand in quantum materials”. en. In: *Nature Materials* 16 (2017), p. 1077. DOI: [10.1038/nmat5017](https://doi.org/10.1038/nmat5017).

[13] A. De La Torre et al. “Colloquium: Nonthermal pathways to ultrafast control in quantum materials”. In: *Reviews of Modern Physics* 93 (2021), p. 041002. DOI: [10.1103/RevModPhys.93.041002](https://doi.org/10.1103/RevModPhys.93.041002).

[14] J. Bloch et al. “Strongly correlated electron–photon systems”. en. In: *Nature* 606 (2022), p. 41. DOI: [10.1038/s41586-022-04726-w](https://doi.org/10.1038/s41586-022-04726-w).

[15] A. Schiffrin et al. “Optical-field-induced current in dielectrics”. en. In: *Nature* 493 (Jan. 2013), p. 70. DOI: [10.1038/nature11567](https://doi.org/10.1038/nature11567).

[16] G. Wachter et al. “Ab Initio Simulation of Electrical Currents Induced by Ultrafast Laser Excitation of Dielectric Materials”. In: *Phys. Rev. Lett.* 113 (2014), p. 087401. DOI: [10.1103/PhysRevLett.113.087401](https://doi.org/10.1103/PhysRevLett.113.087401).

[17] M. Schultze et al. “Controlling dielectrics with the electric field of light”. en. In: *Nature* 493 (2013), p. 75. DOI: [10.1038/nature11720](https://doi.org/10.1038/nature11720).

[18] M. Ossiander et al. “The speed limit of optoelectronics”. en. In: *Nature Communications* 13 (2022), p. 1620. DOI: [10.1038/s41467-022-29252-1](https://doi.org/10.1038/s41467-022-29252-1).

[19] K. A. Cremin et al. “Photoenhanced metastable c-axis electrodynamics in stripe-ordered cuprate  $\text{La}_{1.885}\text{Ba}_{0.115}\text{CuO}_4$ ”. en. In: *Proceedings of the National Academy of Sciences* 116.40 (Oct. 2019), pp. 19875–19879. DOI: [10.1073/pnas.1908368116](https://doi.org/10.1073/pnas.1908368116).

[20] M. A. Cazalilla and J. B. Marston. “Time-Dependent Density-Matrix Renormalization Group: A Systematic Method for the Study of Quantum Many-Body Out-of-Equilibrium Systems”. In: *Phys. Rev. Lett.* 88 (2002), p. 256403. DOI: [10.1103/PhysRevLett.88.256403](https://doi.org/10.1103/PhysRevLett.88.256403).

[21] T. Otobe et al. “First-principles electron dynamics simulation for optical breakdown of dielectrics under an intense laser field”. In: *Phys. Rev. B* 77 (2008), p. 165104. DOI: [10.1103/PhysRevB.77.165104](https://doi.org/10.1103/PhysRevB.77.165104).

[22] D. Hochstuhl and M. Bonitz. “Time-dependent restricted-active-space configuration-interaction method for the photoionization of many-electron atoms”. In: *Phys. Rev. A* 86 (2012), p. 053424. DOI: [10.1103/PhysRevA.86.053424](https://doi.org/10.1103/PhysRevA.86.053424).

[23] D. Hochstuhl, C. M. Hinz, and M. Bonitz. “Time-Dependent Multiconfiguration Methods for the Numerical Simulation of Photoionization Processes of Many-Electron Atoms”. In: *The European Physical Journal Special Topics* 223 (2014), p. 177. DOI: [10.1140/epjst/e2014-02092-3](https://doi.org/10.1140/epjst/e2014-02092-3).

[24] T. Sato et al. “Communication: Time-dependent optimized coupled-cluster method for multielectron dynamics”. In: *The Journal of Chemical Physics* 148 (2018), p. 051101. DOI: [10.1063/1.5020633](https://doi.org/10.1063/1.5020633).

[25] T. B. Pedersen and S. Kvaal. “Symplectic integration and physical interpretation of time-dependent coupled-cluster theory”. In: *The Journal of Chemical Physics* 150 (2019), p. 144106. DOI: [10.1063/1.5085390](https://doi.org/10.1063/1.5085390).

[26] M. Eckstein, M. Kollar, and P. Werner. “Thermalization after an Interaction Quench in the Hubbard Model”. In: *Phys. Rev. Lett.* 103 (2009), p. 056403. DOI: [10.1103/PhysRevLett.103.056403](https://doi.org/10.1103/PhysRevLett.103.056403).

[27] N. Schlünzen, J.-P. Joost, and M. Bonitz. “Achieving the Scaling Limit for Nonequilibrium Green Functions Simulations”. In: *Phys. Rev. Lett.* 124 (2020), p. 076601. DOI: [10.1103/PhysRevLett.124.076601](https://doi.org/10.1103/PhysRevLett.124.076601).

[28] J.-P. Joost et al. “Dynamically screened ladder approximation: Simultaneous treatment of strong electronic correlations and dynamical screening out of equilibrium”. In: *Phys. Rev. B* 105 (2022), p. 165155. DOI: [10.1103/PhysRevB.105.165155](https://doi.org/10.1103/PhysRevB.105.165155).

[29] E. Perfetto, Y. Pavlyukh, and G. Stefanucci. “Real-Time G W : Toward an *Ab Initio* Description of the Ultrafast Carrier and Exciton Dynamics in Two-Dimensional Materials”. en. In: *Physical Review Letters* 128 (2022), p. 016801. DOI: [10.1103/PhysRevLett.128.016801](https://doi.org/10.1103/PhysRevLett.128.016801).

[30] Y. Pavlyukh et al. “Time-linear scaling nonequilibrium Green’s function methods for real-time simulations of interacting electrons and bosons. I. Formalism”. en. In: *Physical Review B* 105 (2022), p. 125134. DOI: [10.1103/PhysRevB.105.125134](https://doi.org/10.1103/PhysRevB.105.125134).

[31] F. Lackner et al. “Propagating two-particle reduced density matrices without wave functions”. In: *Phys. Rev. A* 91 (2015), p. 023412. DOI: [10.1103/PhysRevA.91.023412](https://doi.org/10.1103/PhysRevA.91.023412).

[32] F. Lackner et al. “High-harmonic spectra from time-dependent two-particle reduced-density-matrix theory”. In: *Phys. Rev. A* 95 (2017), p. 033414. DOI: [10.1103/PhysRevA.95.033414](https://doi.org/10.1103/PhysRevA.95.033414).

[33] U. Schollwöck. “The density-matrix renormalization group”. In: *Rev. Mod. Phys.* 77 (2005), p. 259. DOI: [10.1103/RevModPhys.77.259](https://doi.org/10.1103/RevModPhys.77.259).

[34] J. Haegeman et al. “Unifying time evolution and optimization with matrix product states”. In: *Phys. Rev. B* 94 (2016), p. 165116. DOI: [10.1103/PhysRevB.94.165116](https://doi.org/10.1103/PhysRevB.94.165116).

[35] B. Kloss, Y. B. Lev, and D. Reichman. “Time-dependent variational principle in matrix-product state manifolds: Pitfalls and potential”. In: *Phys. Rev. B* 97 (2018), p. 024307. DOI: [10.1103/PhysRevB.97.024307](https://doi.org/10.1103/PhysRevB.97.024307).

[36] J. I. Cirac et al. “Matrix product states and projected entangled pair states: Concepts, symmetries, theorems”. In: *Rev. Mod. Phys.* 93 (2021), p. 045003. DOI: [10.1103/RevModPhys.93.045003](https://doi.org/10.1103/RevModPhys.93.045003).

[37] E. Runge and E. K. U. Gross. “Density-Functional Theory for Time-Dependent Systems”. In: *Phys. Rev. Lett.* 52 (1984), p. 997. DOI: [10.1103/PhysRevLett.52.997](https://doi.org/10.1103/PhysRevLett.52.997).

[38] C. Ullrich. *Time-Dependent Density-Functional Theory: Concepts and Applications*. OUP Oxford, 2012. 541 pp. DOI: [10.1093/acprof:oso/9780199563029.001.0001](https://doi.org/10.1093/acprof:oso/9780199563029.001.0001).

[39] G. Stefanucci and R. van Leeuwen. *Nonequilibrium Many-body Theory of Quantum Systems: A Modern Introduction*. Cambridge University Press, Cambridge, 2025.

[40] S. Donsa et al. “Nonequilibrium Correlation Dynamics in the One-Dimensional Fermi-Hubbard Model: A Testbed for the Two-Particle Reduced Density Matrix Theory”. In: *Physical Review Research* 5 (2023), p. 033022. DOI: [10.1103/PhysRevResearch.5.033022](https://doi.org/10.1103/PhysRevResearch.5.033022).

[41] M. Coppola, M. C. Bañuls, and Z. Lenarčič. “Learning the non-Markovian features of subsystem dynamics”. In: *SciPost Phys.* 19 (2025), p. 149. DOI: [10.21468/SciPostPhys.19.6.149](https://doi.org/10.21468/SciPostPhys.19.6.149).

[42] J. Zhang, C. L. Benavides-Riveros, and L. Chen. “Neural network solution of non-Markovian quantum state diffusion and operator construction of quantum stochastic process”. In: *The Journal of Chemical Physics* 163 (2025), p. 194103. DOI: [10.1063/5.0298594](https://doi.org/10.1063/5.0298594).

[43] W. Liu et al. “Predicting rate kernels via dynamic mode decomposition”. In: *The Journal of Chemical Physics* 159 (2023), p. 144110. DOI: [10.1063/5.0170512](https://doi.org/10.1063/5.0170512).

[44] P. P. Mazza et al. “Machine learning time-local generators of open quantum dynamics”. In: *Phys. Rev. Res.* 3 (2021), p. 023084. DOI: [10.1103/PhysRevResearch.3.023084](https://doi.org/10.1103/PhysRevResearch.3.023084).

[45] L. Chen and Y. Wu. “Learning quantum dissipation by the neural ordinary differential equation”. In: *Physical Review A* 106 (2022). DOI: [10.1103/physreva.106.022201](https://doi.org/10.1103/physreva.106.022201).

[46] C.-S. Chen and E.-J. Kuo. “Unraveling quantum environments: Transformer-assisted learning in Lindblad dynamics”. In: *Phys. Rev. A* 112 (2025), p. 042227. DOI: [10.1103/gsxk-45mk](https://doi.org/10.1103/gsxk-45mk).

[47] E. Genois et al. “Quantum-Tailored Machine-Learning Characterization of a Superconducting Qubit”. In: *PRX Quantum* 2 (2021), p. 040355. DOI: [10.1103/PRXQuantum.2.040355](https://doi.org/10.1103/PRXQuantum.2.040355).

[48] Y. Huang et al. “Direct Entanglement Detection of Quantum Systems Using Machine Learning”. In: *npj Quantum Information* 11.1 (Feb. 20, 2025), p. 29. DOI: [10.1038/s41534-025-00970-w](https://doi.org/10.1038/s41534-025-00970-w).

[49] H. Lange et al. “From architectures to applications: a review of neural quantum states”. In: *Quantum Science and Technology* 9 (2024), p. 040501. DOI: [10.1088/2058-9565/ad7168](https://doi.org/10.1088/2058-9565/ad7168).

[50] L. Ye, Y. Wang, and X. Zheng. “Simulating many-body open quantum systems by harnessing the power of artificial intelligence and quantum computing”. In: *The Journal of Chemical Physics* 162.12 (Mar. 2025), p. 120901. DOI: [10.1063/5.0242648](https://doi.org/10.1063/5.0242648).

[51] Y. Chen and L. You. “Optimal Control of Unknown Collective Spin Systems via a Neural Network Surrogate”. In: *Chinese Physics Letters* 42 (2025), p. 100601. DOI: [10.1088/0256-307X/42/10/100601](https://doi.org/10.1088/0256-307X/42/10/100601).

[52] A. Norambuena et al. “Physics-Informed Neural Networks for Quantum Control”. In: *Phys. Rev. Lett.* 132 (2024), p. 010801. DOI: [10.1103/PhysRevLett.132.010801](https://doi.org/10.1103/PhysRevLett.132.010801).

[53] P. Kidger et al. “Neural Controlled Differential Equations for Irregular Time Series”. In: *Advances in Neural Information Processing Systems*. Ed. by H. Larochelle et al. Vol. 33. Curran Associates, Inc., 2020, pp. 6696–6707. DOI: <https://doi.org/10.48550/arXiv.2005.08926>.

[54] P. Toth et al. “Hamiltonian Generative Networks”. In: *International Conference on Learning Representations*. 2020. DOI: <https://doi.org/10.48550/arXiv.1909.13789>.

[55] J. Morrill et al. “Neural Rough Differential Equations for Long Time Series”. In: *Proceedings of the 38th International Conference on Machine Learning, ICML 2021, 18-24 July 2021, Virtual Event*. Ed. by Marina Meila and Tong Zhang. Vol. 139. Proceedings of Machine Learning Research. PMLR, 2021, p. 7829. DOI: <https://doi.org/10.48550/arXiv.2009.08295>.

[56] F. Dietrich et al. “Learning effective stochastic differential equations from microscopic simulations: Linking stochastic numerics to deep learning”. In: *Chaos* 33 (2023), p. 023121. DOI: [10.1063/5.0113632](https://doi.org/10.1063/5.0113632).

[57] F. Carnazza et al. “Inferring Markovian quantum master equations of few-body observables in interacting spin chains”. In: *New Journal of Physics* 24 (2022), p. 073033. DOI: [10.1088/1367-2630/ac7df6](https://doi.org/10.1088/1367-2630/ac7df6).

[58] F. Carnazza et al. “Machine learning stochastic differential equations for the evolution of order parameters of classical many-body systems in and out of equilibrium”. In: *Machine Learning: Science and Technology* 5 (2024), p. 045002. DOI: [10.1088/2632-2153/ad7ad7](https://doi.org/10.1088/2632-2153/ad7ad7).

[59] M. Schmitt and M. Heyl. “Quantum Many-Body Dynamics in Two Dimensions with Artificial Neural Networks”. In: *Phys. Rev. Lett.* 125 (2020), p. 100503. DOI: [10.1103/PhysRevLett.125.100503](https://doi.org/10.1103/PhysRevLett.125.100503).

[60] S.-H. Lin and F. Pollmann. “Scaling of Neural-Network Quantum States for Time Evolution”. In: *physica status solidi (b)* 259 (2022). DOI: [10.1002/pssb.202100172](https://doi.org/10.1002/pssb.202100172).

[61] H. Zhao et al. *Learning effective Hamiltonians for adaptive time-evolution quantum algorithms*. 2024. arXiv: [2406.06198](https://arxiv.org/abs/2406.06198). URL: <https://arxiv.org/abs/2406.06198>.

[62] N. Mohseni et al. “Deep learning of many-body observables and quantum information scrambling”. In: *Quantum* 8 (2024), p. 1417. DOI: [10.22331/q-2024-07-18-1417](https://doi.org/10.22331/q-2024-07-18-1417).

[63] H. Zeng, Y. Kou, and X. Sun. “How Sophisticated Are Neural Networks Needed to Predict Long-Term Nonadiabatic Dynamics?” In: *Journal of Chemical Theory and Computation* 20 (2024). PMID: 39540684, p. 9832. DOI: [10.1021/acs.jctc.4c01223](https://doi.org/10.1021/acs.jctc.4c01223).

[64] Z. An et al. “Dual-Capability Machine Learning Models for Quantum Hamiltonian Parameter Estimation and Dynamics Prediction”. In: *Phys. Rev. Lett.* 134 (2025), p. 120202. DOI: [10.1103/PhysRevLett.134.120202](https://doi.org/10.1103/PhysRevLett.134.120202).

[65] R. Kaneko et al. “Forecasting long-time dynamics in quantum many-body systems by dynamic mode decomposition”. In: *Phys. Rev. Res.* 7 (2025), p. 013085. DOI: [10.1103/PhysRevResearch.7.013085](https://doi.org/10.1103/PhysRevResearch.7.013085).

[66] Z.-H. Sun et al. “Probing prethermal nonergodicity through measurement outcomes of monitored quantum dynamics”. In: *Phys. Rev. B* 112 (2025), p. L180306. DOI: [10.1103/v4xv-74s7](https://doi.org/10.1103/v4xv-74s7).

[67] M. S. Schmitt et al. *Information theory for data-driven model reduction in physics and biology*. 2025. arXiv: [2312.06608](https://arxiv.org/abs/2312.06608). URL: <https://arxiv.org/abs/2312.06608>.

[68] G. Cemin, M. Schmitt, and M. Bukov. *Learning to stabilize nonequilibrium phases of matter with active feedback using partial information*. 2025. arXiv: [2508.06612](https://arxiv.org/abs/2508.06612). URL: <https://arxiv.org/abs/2508.06612>.

[69] R. T. Q. Chen et al. “Neural Ordinary Differential Equations”. In: *Advances in Neural Information Processing Systems*. Ed. by S. Bengio et al. Vol. 31. Curran Associates, Inc., 2018. URL: [https://proceedings.neurips.cc/paper\\_files/paper/2018/file/69386f6bb1dfed68692a24c8686939b9-Paper.pdf](https://proceedings.neurips.cc/paper_files/paper/2018/file/69386f6bb1dfed68692a24c8686939b9-Paper.pdf).

[70] Z. Qian et al. “Integrating Expert ODEs into Neural ODEs: Pharmacology and Disease Progression”. In: *Advances in Neural Information Processing Systems*. Ed. by M. Ranzato et al. Vol. 34. Curran Associates, Inc., 2021, p. 11364. URL: [https://proceedings.neurips.cc/paper\\_files/paper/2021/file/5ea1649a31336092c05438df996a3e59-Paper.pdf](https://proceedings.neurips.cc/paper_files/paper/2021/file/5ea1649a31336092c05438df996a3e59-Paper.pdf).

[71] J. M. Worsham and J. K. Kalita. “A Guide to Neural Ordinary Differential Equations: Machine Learning for Data-Driven Digital Engineering”. In: *Digital Engineering* 6 (2025), p. 100060. DOI: [10.1016/j.dte.2025.100060](https://doi.org/10.1016/j.dte.2025.100060).

[72] M. Höge et al. “Improving hydrologic models for predictions and process understanding using neural ODEs”. In: *Hydrology and Earth System Sciences* 26 (2022), p. 5085. DOI: [10.5194/hess-26-5085-2022](https://doi.org/10.5194/hess-26-5085-2022).

[73] H. Aliee, F. J. Theis, and N. Kilbertus. *Beyond Predictions in Neural ODEs: Identification and Interventions*. 2025. arXiv: [2106.12430](https://arxiv.org/abs/2106.12430). URL: <https://arxiv.org/abs/2106.12430>.

[74] K. Lee and E. J. Parish. “Parameterized Neural Ordinary Differential Equations: Applications to Computational Physics Problems”. In: *Proceedings of the Royal Society A: Mathematical, Physical and Engineering Sciences* 477 (2021), p. 20210162. DOI: [10.1098/rspa.2021.0162](https://doi.org/10.1098/rspa.2021.0162).

[75] H. Niu et al. “On the Applications of Neural Ordinary Differential Equations in Medical Image Analysis”. In: *Artificial Intelligence Review* 57 (2024), p. 236. DOI: [10.1007/s10462-024-10894-0](https://doi.org/10.1007/s10462-024-10894-0).

[76] F. Sorourifar et al. “Physics-Enhanced Neural Ordinary Differential Equations: Application to Industrial Chemical Reaction Systems”. In: *Industrial & Engineering Chemistry Research* 62 (2023), p. 15563. DOI: [10.1021/acs.iecr.3c01471](https://doi.org/10.1021/acs.iecr.3c01471).

[77] D. S. Bräm et al. “Low-Dimensional Neural ODEs and Their Application in Pharmacokinetics”. In: *Journal of Pharmacokinetics and Pharmacodynamics* 51 (2024), p. 123. DOI: [10.1007/s10928-023-09886-4](https://doi.org/10.1007/s10928-023-09886-4).

[78] M. Choi et al. “Learning quantum dynamics with latent neural ordinary differential equations”. In: *Phys. Rev. A* 105 (2022), p. 042403. DOI: [10.1103/PhysRevA.105.042403](https://doi.org/10.1103/PhysRevA.105.042403).

[79] Koji Hashimoto, Hong-Ye Hu, and Yi-Zhuang You. “Neural ordinary differential equation and holographic quantum chromodynamics”. In: *Machine Learning: Science and Technology* 2.3 (May 2021), p. 035011. DOI: [10.1088/2632-2153/abe527](https://doi.org/10.1088/2632-2153/abe527).

[80] T. Heightman, E. Jiang, and A. Acín. “Solving the quantum many-body Hamiltonian learning problem with neural differential equations”. In: *Quantum Science and Technology* 10 (2025), p. 045072. DOI: [10.1088/2058-9565/ae0d79](https://doi.org/10.1088/2058-9565/ae0d79).

[81] J. Nelson et al. “Data-driven time propagation of quantum systems with neural networks”. In: *Phys. Rev. B* 106 (2022), p. 045402. DOI: [10.1103/PhysRevB.106.045402](https://doi.org/10.1103/PhysRevB.106.045402).

[82] S. J. Wetzel et al. *Interpretable Machine Learning in Physics: A Review*. 2025. arXiv: [2503.23616](https://arxiv.org/abs/2503.23616). URL: <https://arxiv.org/abs/2503.23616>.

[83] M. Qin et al. “The Hubbard Model: A Computational Perspective”. In: *Annual Review of Condensed Matter Physics* 13 (2022), p. 275. DOI: [10.1146/annurev-conmatphys-090921-033948](https://doi.org/10.1146/annurev-conmatphys-090921-033948).

[84] I. Bloch, J. Dalibard, and S. Nascimbène. “Quantum simulations with ultracold quantum gases”. In: *Nature Physics* 8 (2012), p. 267. DOI: [10.1038/nphys2259](https://doi.org/10.1038/nphys2259).

[85] W. Kutzelnigg and D. Mukherjee. “Cumulant expansion of the reduced density matrices”. In: *The Journal of Chemical Physics* 110 (1999), p. 2800. DOI: [10.1063/1.478189](https://doi.org/10.1063/1.478189).

[86] R. T. Q. Chen. *torchdiffeq*. 2018. URL: <https://github.com/rtqichen/torchdiffeq>.

[87] M. Guo, H. Li, and Y. Weng. *Efficient Manifold-Constrained Neural ODE for High-Dimensional Datasets*. 2025. arXiv: [2510.04138](https://arxiv.org/abs/2510.04138). URL: <https://arxiv.org/abs/2510.04138>.

[88] Z. Lai et al. “Neural Modal Ordinary Differential Equations: Integrating Physics-Based Modeling with Neural Ordinary Differential Equations for Modeling High-Dimensional Monitored Structures”. In: *Data-Centric Engineering* 3 (2022), e34. DOI: [10.1017/dce.2022.35](https://doi.org/10.1017/dce.2022.35).

[89] A. Norcliffe et al. *Neural ODE Processes*. 2021. arXiv: [2103.12413](https://arxiv.org/abs/2103.12413). URL: <https://arxiv.org/abs/2103.12413>.

[90] A. Sholokhov et al. “Physics-Informed Neural ODE (PINODE): Embedding Physics into Models Using Collocation Points”. In: *Scientific Reports* 13 (2023), p. 10166. DOI: [10.1038/s41598-023-36799-6](https://doi.org/10.1038/s41598-023-36799-6).

[91] K. Pearson. “VII. Mathematical contributions to the theory of evolution.—III. Regression, heredity, and panmixia”. In: *Philosophical Transactions of the Royal Society of London, Series A: Containing Papers of a Mathematical or Physical Character* 187 (1896), p. 253. DOI: [10.1098/rsta.1896.0007](https://doi.org/10.1098/rsta.1896.0007).

- [92] C. Garrod and J. K. Percus. “Reduction of the N-Particle Variational Problem”. In: *Journal of Mathematical Physics* 5 (1964), p. 1756. DOI: [10.1063/1.1704098](https://doi.org/10.1063/1.1704098).
- [93] A. J. Coleman. “Structure of Fermion Density Matrices”. In: *Rev. Mod. Phys.* 35 (1963), p. 668. DOI: [10.1103/RevModPhys.35.668](https://doi.org/10.1103/RevModPhys.35.668).
- [94] D. A. Mazziotti. “Structure of Fermionic Density Matrices: Complete  $N$ -Representability Conditions”. In: *Phys. Rev. Lett.* 108 (2012), p. 263002. DOI: [10.1103/PhysRevLett.108.263002](https://doi.org/10.1103/PhysRevLett.108.263002).
- [95] E. Pescoller, M. Eder, and I. B řezinová. “Projective purification of correlated reduced density matrices”. In: *Phys. Rev. Res.* 7 (2025), p. 013211. DOI: [10.1103/PhysRevResearch.7.013211](https://doi.org/10.1103/PhysRevResearch.7.013211).
- [96] A. White et al. “Stabilized Neural Differential Equations for Learning Dynamics with Explicit Constraints”. In: *Advances in Neural Information Processing Systems*. Ed. by A. Oh et al. Vol. 36. Curran Associates, Inc., 2023, p. 12929. URL: [https://proceedings.neurips.cc/paper\\_files/paper/2023/file/2a4179ef39846557e99f6bfac580ea2e-Paper-Conference.pdf](https://proceedings.neurips.cc/paper_files/paper/2023/file/2a4179ef39846557e99f6bfac580ea2e-Paper-Conference.pdf).